PROCEEDINGS OF SCIENCE

# Hitomi HXT deconvolution imaging of the Crab Nebula

---

**Mikio Morii,**[a,b,*] **Yoshitomo Maeda,**[a] **Hisamitsu Awaki,**[c] **Kouichi Hagino,**[d] **Manabu Ishida**[a] **and Koji Mori**[e]

[a] *Institute of Space and Astronautical Science, Japan Aerospace Exploration Agency, 3-1-1 Yoshinodai, Chuo-ku, Sagamihara, Kanagawa 252-5210, Japan*

[b] *DATUM STUDIO Company Limited, Toranomon Hills Business Tower 27F, 1-17-1 Toranomon, Minato-ku, Tokyo 105-6427, Japan*

[c] *Department of Physics, Ehime University, 2-5 Bunkyou-cho, Matsuyama, Ehime 790-8577, Japan*

[d] *Department of Physics, The University of Tokyo, 7-3-1 Hongou, Bunkyo-ku, Tokyo 113-0033, Japan*

[e] *epartment of Applied Physics and Electronic Engineering, University of Miyazaki, Miyazaki 889-2192, Japan*

*E-mail:* `morii.mikio@jaxa.jp`

We develop a new deconvolution method to recover the Crab Nebula image taken by the Hitomi/HXT. To suppress the artifact due to the bright Crab pulsar located at the center of the Crab Nebula, we extend the Richardson-Lucy method. Here, we introduce two components corresponding to the nebula and pulsar with regularization for smoothness and flux, respectively, and we perform combined deconvolution of multi-pulse-phase images. At 3.6-15 keV band, we successfully recover the structures of torus and jets, as seen in the Chandra X-ray image. Above 15 keV, we confirm the NuSTAR's findings that the nebula size decreases in higher energy bands.

*Frontier Research in Astrophysics – IV (FRAPWS2024)*
*9-14 September 2024*
*Mondello, Palermo, Italy*

PoS(FRAPWS2024)048

---

[*] Speaker

## 1. Introduction

The Crab Nebula is a remnant of a supernova SN 1054 located at Taurus. There is a rapidly spinning neutron star, a pulsar, with a period of 34 ms at the center of the nebula. High energy accelerated particles are generated by the rotational energy loss of the pulsar ($10^{39}$ ergs $s^{-1}$), producing synchrotron X-ray nebula. Its X-ray image is important to know particle acceleration mechanism. But, no images with an angular resolution of arcsec is obtained above 10 keV.

The *Hitomi* X-ray Observatory (launched in 2016 February and halted its operation at the end of March [11]) carried the hard X-ray imaging spectroscopy system consisting of two pairs of Hard X-ray Imagers (HXI-1 and HXI-2) and Hard X-ray Telescopes (HXT-1 and HXT-2). The HXIs provide images and spectra up to 80 keV with a moderate energy resolution. The angular resolution of the *Hitomi* HXT was reported to be $\sim$ 1.6 arcmin in HPD [5], comparable to that of *NuSTAR*.

*Hitomi* observed the Crab Nebula on 2016 March 25 during *Hitomi*'s commissioning phase, imaging it at around the center of the HXI array. The observation time was $\sim$ 8 ks. It is the only observation of the Crab Nebula by *Hitomi* in its lifetime. We divide the HXI data into three energy bands: 3.6–15, 15–30, and 30–70 keV. Below 15 keV, HXI-2 has noisy lines, so we use only HXI-1 data for 3.6–15 keV band image. The number of photons in these bands are $1.7 \times 10^6$, $4.3 \times 10^5$, and $8.4 \times 10^4$, respectively.

## 2. Image recovery of X-ray distribution at the sky

We perform image recovery of the Crab Nebula observed by *Hitomi*/HXT. Figure 1 shows a conceptual view of the image recovery. It is an inference of X-ray distribution at the sky from the observed X-ray distribution on the camera, so-called inverse problem. Here, we consider the following conditions. (1) Since the X-ray distribution at the sky is the superposition of point sources, X-ray distribution on the camera is the superposition of the point spread function (PSF). (2) When the average number of X-ray photons detected on a camera pixel is $\mu$, the number of X-ray photons at the pixel ($Y$) follow Poisson probability distribution with mean of $\mu$. (3) The number of X-ray photons at each camera pixel ($Y$) is a random variable and mutually independent. (4) X-ray distribution at the sky consists of two components: pulsar component (point source) and nebula component. (5) Pulsar component has periodical time variation, while nebula component has no time variation. (6) Nebula component has a smooth distribution. By taking these conditions into account, we infer the most likely X-ray distribution at the sky by the image deconvolution.

## 3. Point spread function

For the image deconvolution, PSFs as a function of directions of incoming photons (response matrix) is necessary, however the PSF of *Hitomi* is not well modeled due to its short life. Fortunately a reliable PSF can be obtained for the Crab Nebula as demonstrated by Matsumoto et al. [5]. Here, PSF is made by the operation of image subtraction of pulse phase ON - OFF. We assume the same PSF for off-axis directions as that of on-axis direction. We make the response matrix by copying such a PSF at the locations every 1.77 arcsec spacing. PSF core of HXT is sharp (~9 arcsec). So, image with high angular resolution is expected to be made by image deconvolution.

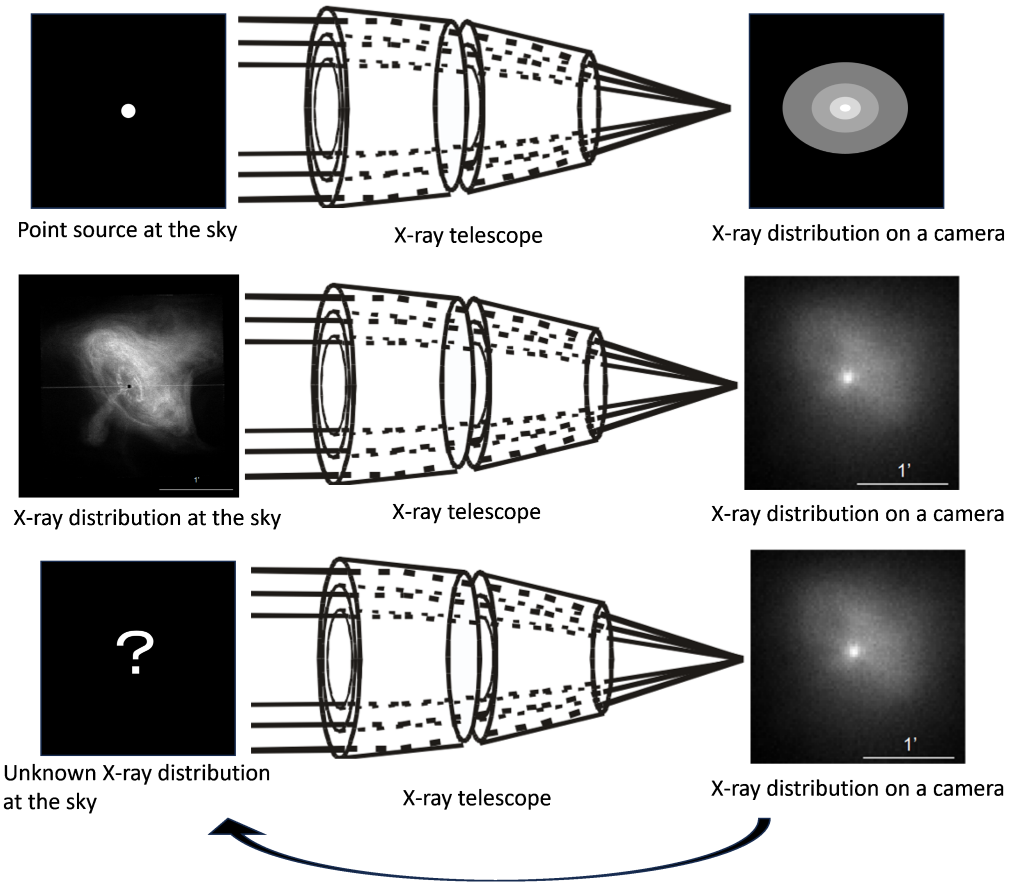

**Figure 1:** (Upper panel:) X-ray photons from a point source at the sky go through X-ray telescope and are detected at the camera on the focal plane. Here, the X-ray photons at the camera spread as shown in the right-hand side. The distribution on the camera is the point spread function (PSF). (Middle:) X-ray distribution at the sky is the superposition of point sources, so the X-ray distribution on the camera is the superposition of the PSF. (Bottom:) We perform an inference of X-ray distribution at the sky from the observed X-ray distribution on the camera.

## 4. Combined multi-pulse-phase image deconvolution

Image deconvolution is a method to recover an original image from an observed image blurred by instrumental factors such as the PSF of a telescope. The Richardson-Lucy method [9, 10] is a canonical method for image deconvolution. It obtain the image with a maximal likelihood for given image data, assuming that the detected photon events follow the Poisson distribution. Since the Crab Nebula is a spatially extended object, Bayesian inference is necessary to introduce smoothness. Since the pulsar is very bright, simple smoothing operation would make pulsar's photons spread out over nebula [7]. Then we develop a new deconvolution method specifically tuned for the Crab Nebula.

We assume two components for the sky image: the point source and extended smooth components. By introducing simultaneous image deconvolution using the images of all pulse phases at once, decoupling of two components is clarified further. We divide the observed data into $n_p$

pulse phases ($n_p = 10$) and extract an image for each pulse-phase bin. Here, pulse phases are indexed with $p = 1, 2, \cdots, n_p$, and the ratio of the time width of phase $p$ to the pulse period is $(\Delta\phi)_p = 1/n_p$. We express the image of the Crab Nebula with $I_u$ and the Crab pulsar with $I_{0,u}$, where the value of $I_{0,u}$ is one at the position of the Crab pulsar and zero at the other positions. The intensity of the Crab pulsar at phase $p$ is $f_p$. Then, the number of events in pixel $v$ of counter $c$ in an exposure of pulse phase $p$ ($Y_{c,p,v}$) follows a Poisson distribution:

$$Y_{c,p,v} \sim \text{Poisson}\left\{\left[\sum_u t_{c,v,u}(I_u + f_p I_{0,u}) + b_{c,v}\right](\Delta\phi)_p (F_{\text{lt}})_{c,p}\right\}, \tag{1}$$

where $t_{c,v,u}$ is the response of the *Hitomi*-HXT/HXI. It means a distribution of the expected photon counts at pixel $v$ of counter $c$ originating from a unit intensity of photons at pixel $u$ on the sky, that is the PSF. $b_{c,v}$ is a non-negative real value of the particle background counts at pixel $v$ of counter $c$. $(F_{\text{lt}})_{c,p}$ is the fraction of the livetime to an exposure of pulse phase $p$ for HXI $c$. Thus, the likelihood of detecting $Y$ events given $I$ and $f$ is expressed by:

$$p(Y|I,f) = \prod_{c=1}^{n_c}\prod_{p=1}^{n_p}\prod_{v=1}^{V} \text{Poisson}\left\{Y_{c,p,v}; \left[\sum_u t_{c,v,u}(I_u + f_p I_{0,u}) + b_{c,v}\right](\Delta\phi)_p (F_{\text{lt}})_{c,p}\right\}. \tag{2}$$

## 5. Regularization

We introduce a smoothness constraint on the nebula component $I_u$ to reduce statistical fluctuations and to decouple the nebula and pulsar components at the pulsar position. The prior probability for $I_u$ is

$$p_{\text{smooth}}(I) = Z_I \exp[-\mu V(I)], \tag{3}$$

where $Z_I$ is a normalization constant, $\mu > 0$ is a hyper-parameter for the smoothness of the nebula component and

$$\begin{aligned} V(I) &= \sum_{(r,s)\in N} (I_r - I_s)^2 \\ &= \sum_{i=1}^{m-1}\sum_{j=1}^{n-1}\left[(I_{i,j} - I_{i+1,j})^2 + (I_{i,j} - I_{i,j+1})^2\right] + \sum_{i=1}^{m-1}(I_{i,n} - I_{i+1,n})^2 + \sum_{j=1}^{n-1}(I_{m,j} - I_{m,j+1})^2 \end{aligned} \tag{4}$$

Here, $\sum_{(r,s)\in N}$ denotes the summation between two adjoining pixels.

We also introduce the flux constraint on the pulsar flux $f_p$. The prior probability for $f_p$ is

$$p_{\text{flux}}(f) = Z_f \exp[-\gamma D(f)], \tag{5}$$

where $Z_f$ is a normalization constant and

$$D(f) = \sum_p (f_p - f_{0,p})^2. \tag{6}$$

Here, the $\gamma > 0$ is a hyper-parameter to keep the flux value close to the pulsed flux of the Crab pulsar $f_{0,p}$. The $\gamma$ parameter works to adjust the difference between the pulsed and total fluxes of the Crab pulsar. The pulsed flux $f_{0,p}$ is obtained with

$$f_{0,p} = \frac{1}{(\Delta\phi)_p}\sum_c \frac{\sum_v Y_{c,p,v}}{(F_{\text{lt}})_{c,p}} - \frac{1}{(\Delta\phi)_{\text{off}}}\sum_c \frac{\sum_v Y_{c,\text{off},v}}{(F_{\text{lt}})_{c,\text{off}}}, \tag{7}$$

where the suffix "off" indicates the minimum-intensity pulse phase.

## 6. Posterior probability and optimization

The posterior probability is obtained with

$$p(I, f|Y) = \frac{p(I, f, Y)}{p(Y)} = \frac{p_{\mathrm{smooth}}(I) p_{\mathrm{flux}}(f) p(Y|I, f)}{p(Y)}. \tag{8}$$

We solve this for $I$ and $f$ by maximizing the logarithm of $p(I, f|Y)$:

$$\begin{aligned} \log p(I, f|Y) &= \log p(Y|I, f) + \log p_{\mathrm{smooth}}(I) + \log p_{\mathrm{flux}}(f) + \mathrm{const.} \\ &= \log p(Y|I, f) - \mu V(I) - \gamma D(f) + \mathrm{const.} \end{aligned} \tag{9}$$

We use the Expectation-Maximization (EM) algorithm [1, 2] to maximize the likelihood part $p(Y|I, f)$. Combining prior-probability parts, we apply the Majorization-Minimization (MM) algorithm [3]. Here, we show conceptual view of the algorithm by Figure 2. The detailed explanation is shown in [8].

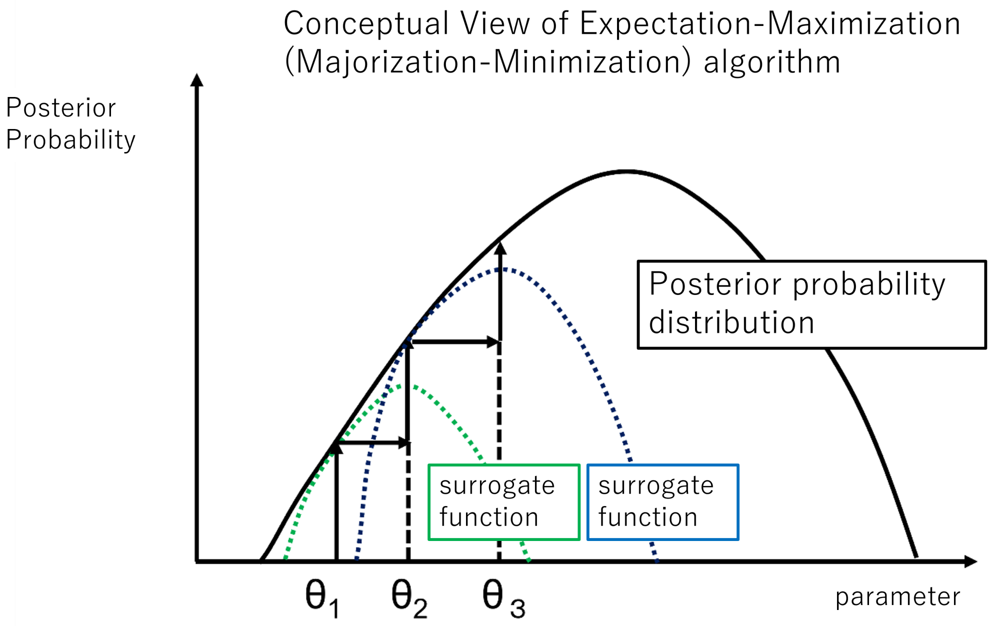

**Figure 2:** Conceptual view of EM algorithm: In this figure, horizontal and vertical axes are parameter and posterior probability, respectively. Solid line shows posterior probability distribution. At the first step, the parameter is at $\theta_1$. Here, we can calculate a surrogate function (green dotted line), which is an infimum of the posterior probability distribution. We optimize the parameter $\theta$ with respect to the surrogate function, then reach at the next parameter $\theta_2$. The posterior probability has increased from $\theta_1$ to $\theta_2$. In the similar way, posterior probability increases by the step of $\theta_3$, $\theta_4$, . . . .

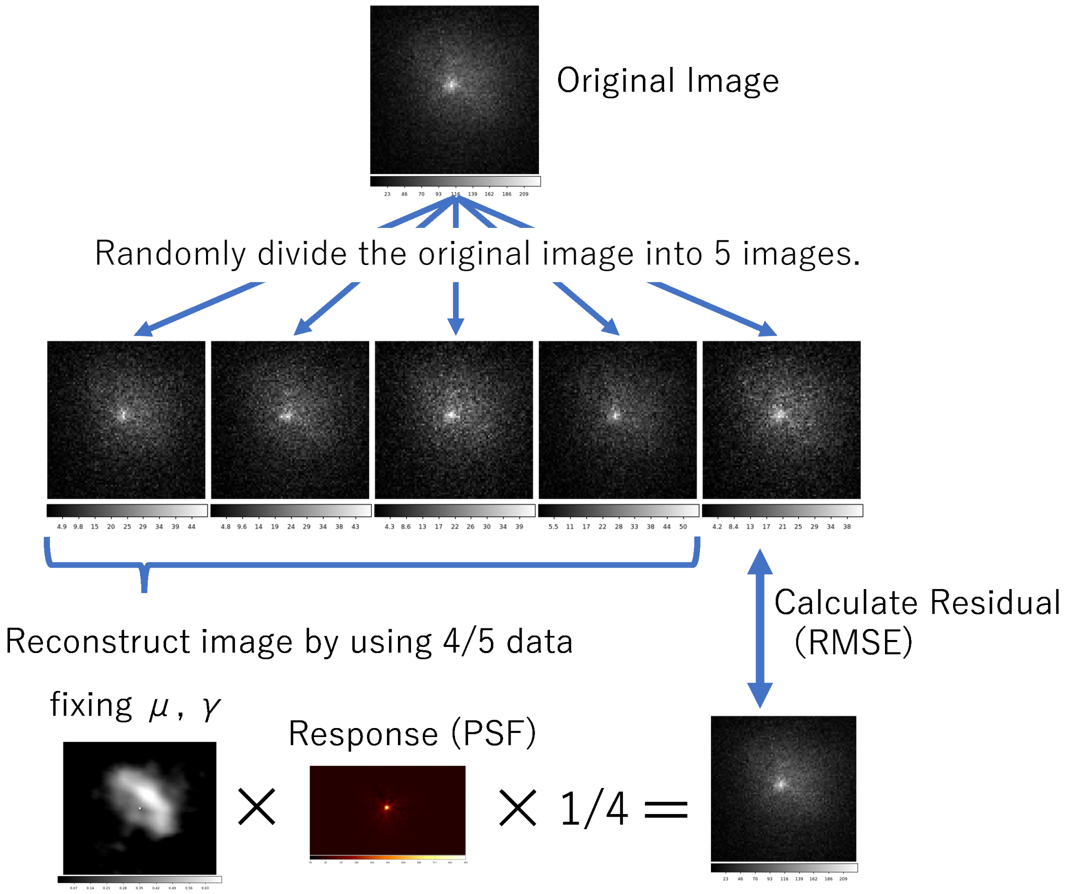

**Figure 3:** Flow of cross-validation of hyper-parameter.

## 7. Cross-validation of hyper-parameter

Hyper-parameter $\mu$ and $\gamma$ are determined by the five-fold cross validation as shown in Figure 3. Original image is randomly divided into five random images, where each random image contains 1/5 photons of the original image. Using the data of four of the five random images, we perform our image deconvolution with fixing $\mu$ and $\gamma$ parameters. By multiplying the response matrix (point spread function) with the obtained deconvolved image and multiplying the factor 1/4, we obtain the simulated image at the detector which should be similar with the remaining one random image. The difference between these images can be evaluated by calculating RMSE. By changing the combination of four random images among the five random images, and following the same calculation, we can obtain five RMSE values. Means and standard deviations for the five RMSE values are calculated for each $\mu$ and $\gamma$ hyper-parameter.

Since $\gamma$ parameter has little effect on the nebula image, we adopt the value with the smallest RMSE for this parameter. For the $\mu$ parameter, we adopt the one-standard error rule to avoid over-training for the training data. In this rule, we adopt the largest permitted $\mu$ (i.e., the smoothest) parameter within fluctuations of the RMSE. We search the parameter among 121 pairs of ($\mu$, $\gamma$), where $\log_{10}\mu$ and $\log_{10}\gamma$ are varied from $-10$ to 0 by a step of 1.

## 8. Results

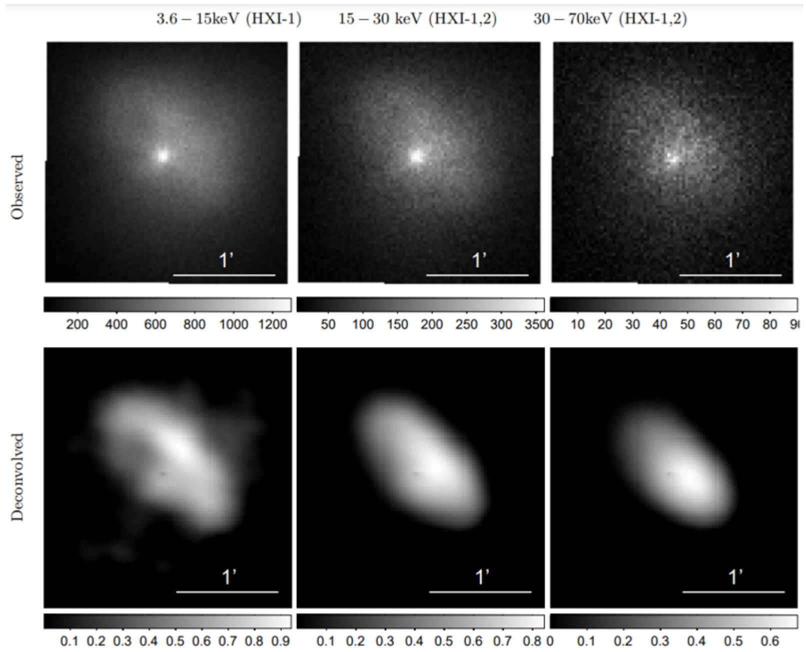

**Figure 4:** The observed and deconvolved images of the Crab Nebula obtained by the *Hitomi* HXI in three energy bands. The upper and lower rows show the observed images taken by the HXI and the deconvolved images without the pulsar component, respectively. The left panels show the 3.6 – 15 keV band images based on the HXT-1 data. The center and right panels show the 15 – 30 keV and 30 – 70 keV band images, respectively, based on both the HXT-1 and HXT-2 data.

We apply our deconvolution method to the *Hitomi*/HXT data for three energy bands of 3.6 – 15, 15 – 30, and 30 – 70 keV. The observed energy-separated *Hitomi* HXI images are shown in the upper panels of figure 4. We determine the best hyper-parameters with the cross-validation and then perform the deconvolution with the best hyper-parameters. The resultant deconvolved images are shown in the lower panels of figure 4. Figure 4 shows that emission region becomes smaller in higher energy band.

Figure 5 shows a comparison between our deconvolved image in the 3.6 – 15 keV band and *Chandra* ACIS 0.5 – 7.0 keV band image [6]. Our *Hitomi* HXI image appears similar to the *Chandra* image. The torus, south-east jet, and north-west extended emission of the Crab Nebula are clearly seen in our deconvolved image.

## 9. Summary

In our image deconvolution for the Crab nebula taken by Hitomi/HXT, we made the point spread function from an image operation of ON - OFF of the Crab pulsar image. Then, we can obtain a reliable point spread function. We have improved the image deconvolution method from the Richardson-Lucy method in the following points: (1) We have introduced smoothness and flux regularization based on Bayesian inference; (2) To reduce the artifact due to the bright point source,

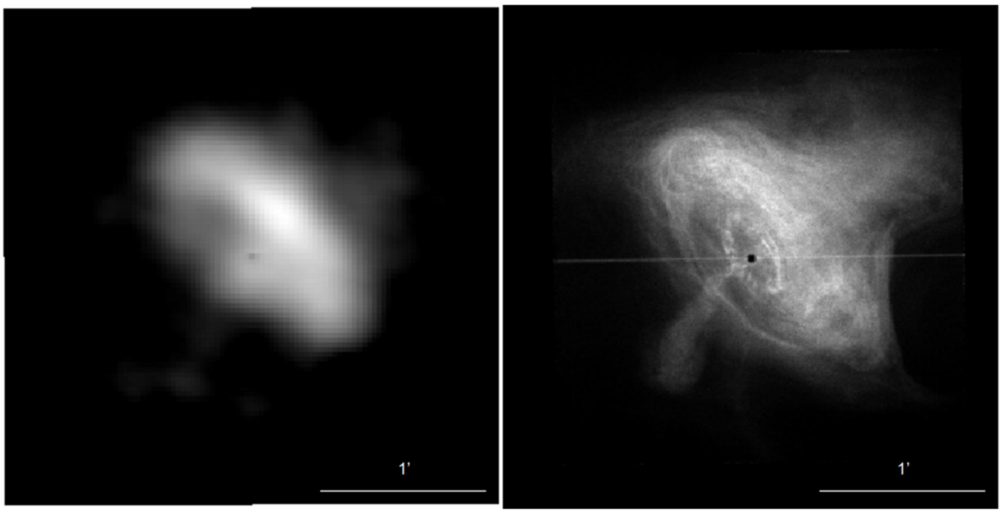

**Figure 5:** Comparison between the deconvolved *Hitomi* HXI-1 3.6 – 15 keV band image (left panel) and *Chandra* ACIS 0.5 – 7.0 keV band image (right panel).

Crab pulsar, we have introduced two components: pulsar flux component and nebula component; (3) We have performed combined multi-pulse-phase image deconvolution. Below 15 keV, torus and jets are seen in the deconvolved image. Above 15 keV, nebula looks like a torus structure and jets are not seen. Emission region becomes smaller in higher energy band. It is consistent with the NuSTAR results [4]. Details of our work are shown in [8].

## References

[1] Bishop, C. M. 2006, Pattern Recognition and Machine Learning (New York: Springer New York)

[2] Dempster, A. P., Laird, N. M., & Rubin, D. B. 1977, Journal of the Royal Statistical Society, Series B (Methodological), 39, 1

[3] Hunter, D. R., & Lange, K. 2000, Journal of Computational and Graphical Statistics, 9, 60

[4] Madsen, K. K., et al. 2015, The Astrophysical Journal, 801, 66

[5] Matsumoto, H., et al. 2018, Journal of Astronomical Telescopes, Instruments, and Systems, 4, 011212

[6] Mori, K., Burrows, D. N., Hester, J. J., Pavlov, G. G., Shibata, S., & Tsunemi, H. 2004, The Astrophysical Journal, 609, 186

[7] Morii, M., Ikeda, S., & Maeda, Y. 2019, Publications of the Astronomical Society of Japan, 71, 24

[8] Morii, M. et al. 2024, Publications of the Astronomical Society of Japan, 76, 272

[9] Lucy, L. B. 1974, Astronomical Journal, 79, 745

[10] Richardson, W. H. 1972, Journal of the Optical Society of America, 62, 55]

[11] Takahashi, T., et al. 2016, Proceedings of SPIE, 9905, 99050U